PNAS RESEARCH ARTICLE | PLANT BIOLOGY

Split-YFP-coupled interaction–dependent TurboID identifies new functions of basal cell polarity in *Arabidopsis*

Aobo Huang[a,b], Jinming Zhang[a,b], Zhendong Liu[a], Vanessa Schoen[c], Deepanjali Verma[a], Haiyan Zheng[d], Ullas V. Pedmale[c], and Juan Dong[a,b,e,1]

Edited by Joseph Kieber, The University of North Carolina at Chapel Hill, Chapel Hill, NC; received January 31, 2025; accepted June 26, 2025

The formation of a body axis is one of the fundamental steps in developmental patterning in multicellular organisms. Ectopic expression of the stomatal protein BASL (BREAKING OF ASYMMETRY IN THE STOMATAL LINEAGE) reveals a proximal–distal cell polarity field in the leaf and an apical–basal field in the hypocotyl and root of *Arabidopsis*. This provides a framework for uncovering molecular components of body-axis cell polarity in higher plants. In this study, we developed a proximity labeling-based complementation system, termed tSYID (tandem fusion of Split-YFP and TurboID), to enable simultaneous visualization and identification of the tissue-wide cell polarity module marked by interacting BASL and BREVIS RADIX-LIKE 2 (BRXL2) proteins in *Arabidopsis*. This contact-based tSYID system focuses on identifying the protein interactome proximal to the protein–protein interaction site. By combining proximity labeling and mass spectrometry, we identified protein candidates associated with the tSYID-BASL/BRXL2 module, many of which remain uncharacterized in plants. Among them, an AGC protein kinase displayed highly polarized localization at the basal membrane in the hypocotyl and root. Knocking out two close *AGC* homologs in *Arabidopsis* resulted in compromised hypocotyl growth in the dark, suggesting a functional connection between basal cell polarity and plant upward growth. Our study demonstrates the power of using the Split-TurboID strategy to uncover proximal proteomes near protein activity sites and highlights an underappreciated crosstalk between developmentally programmed body axes and environmentally influenced growth vectors.

Arabidopsis | body-axis polarity | proximity labeling | Split-TurboID

Significance

The ability of plants to grow and develop relies on the establishment of body axes, which define directions like top and bottom or inside and outside. This study introduces a proximity labeling tool based on Split-TurboID, termed tSYID, to map protein interactions that create these directional cues in *Arabidopsis*, a model plant. Using this tool, we identified key proteins, including AGC (PKA, PKG, and PKC) kinases, that help guide upward growth. When these proteins are missing, plants fail to grow properly in the dark, revealing a connection between their internal polarity and environmental responses. This research provides an approach to studying how plants organize their cells and adapt their growth, offering insights relevant to agriculture and developmental biology.

Cell polarity is characterized by the uneven distribution of cellular components within a cell. This fundamental feature enables cells to organize and function in a coordinated manner, contributing to the formation of tissues and organs in multicellular organisms. For example, in asymmetric cell division, cell polarity establishes distinct cellular regions, resulting in daughter cells with different sizes, contents, and fates. This process is vital for generating cell-type diversity during development (1, 2). Polarized cells also enable the organization of tissues and the formation of complex structures. This is exemplified by the planar cell polarity (PCP) system, which utilizes inter- and intracellular feedback regulation to align the orientation of cells along the global plane of the tissue—a process critical for creating organized and functional body structures (3–5). In plants, the molecular pathways of PCP are not well defined, partly due to the absence of counterparts to the conserved core PCP components, as well as the existence of multidirectional polarity associated with developmental patterning in plant organs (6). For example, at the whole-body level, auxin transporters, particularly the PIN-FORMED (PIN) proteins, are differentially polarized to direct auxin flow, promoting the formation of auxin gradients and controlling the directionality of cell growth and overall developmental patterning (7, 8). More recently, the discovery of the DIX-domain-containing SOSEKI protein family, whose members localize to polar cell edges pointing inward or outward, has revealed global polarity cues in the model plant *Arabidopsis* (9). Interestingly, the convergence of cell polarity on the DIX-domain-mediated protein oligomerization appears to be a shared feature in both plants and animals (10).

One of the cell polarity regulators associated with asymmetric cell division in *Arabidopsis* is BREAKING ASYMMETRY IN THE STOMATAL LINEAGE (BASL), whose polarization directs the orientation of cell division and asymmetric daughter-cell fate in the stomatal lineage (11). Although BASL is considered to be a stomatal-specific regulator, its physical partners from the BREVIS RADIX (BRX) family play critical roles in root protophloem differentiation by polarizing toward the rootward (basal) side of developing protophloem sieve elements (12). Ectopic expression of BASL throughout the leaf or native expression of BRXL2 revealed a tissue-wide polarity bias toward proximal and medial orientation in the leaf epidermis (13) (*SI Appendix*, Fig. S1 *A* and *B*),

Author affiliations: [a]The Waksman Institute of Microbiology, Rutgers, The State University of New Jersey, Piscataway, NJ 08854; [b]Department of Biochemistry and Biophysics, College of Life and Agricultural Sciences, Texas A&M University, College Station, TX 77843; [c]Cold Spring Harbor Laboratory, Cold Spring Harbor, NY 11724; [d]Biological Mass Spectrometry Facility, Robert Wood Johnson Medical School and Rutgers, The State University of New Jersey, Piscataway, NJ 08854; and [e]Department of Plant Biology, Rutgers, The State University of New Jersey, New Brunswick, NJ 08901

Author contributions: A.H. and J.D. designed research; A.H., J.Z., Z.L., V.S., D.V., and H.Z. performed research; A.H., H.Z., U.V.P., and J.D. analyzed data; and A.H. and J.D. wrote the paper.

The authors declare no competing interest.

This article is a PNAS Direct Submission.

[1]To whom correspondence may be addressed. Email: juan.dong@ag.tamu.edu.

This article contains supporting information online at https://www.pnas.org/lookup/suppl/doi:10.1073/pnas.2502445122/-/DCSupplemental.

Published August 6, 2025.

reflecting an intrinsic mechanical feature associated with leaf expansion and development (13–15). Ectopic expression of BASL in the hypocotyl cells exhibits a basal-lateral polarization pattern, and its activity was connected to regional cell expansion (11). The tissue-wide polarity field of ectopic GFP-BASL extends to the root and becomes more evidently oriented toward the basal side of the plant (see below). However, the biological significance of this rootward polarity field across hypocotyl to root in plant development and growth remains enigmatic.

TurboID-based proximity labeling of cytosolic proteins coupled with mass spectrometry (MS) provides a powerful tool for identification of protein interactions, neighborhoods, and organellar proteomes in living cells, including higher plants (16–18). In the presence of biotin, TurboID catalyzes the covalent attachment of biotin molecules to proteins within its vicinity (19). The specificity for this promiscuous enzyme for detecting spatial proteomes was further enhanced by the development of Split-TurboID, where the enzyme's activity is triggered by the reassembly of its two inactive fragments through protein–protein interaction or organelle contact (20). The application of TurboID in cell polarity studies has been successful in spatially resolving proteomics of the two ends of stomatal lineage cells (21). However, isolating components associated with basal cell polarity, as indicated by GFP-BASL in the hypocotyl and root, is complicated by the significant accumulation of BASL proteins in the nucleus, where no regulatory roles of BASL have been identified (11, 22). To address this, we developed a tandem Split-YFP and TurboID (tSYID) system, leveraging the contact-based Split-TurboID approach. This system allows for the simultaneous visualization of the BASL–BRXL2 interaction and the identification of the proximal proteome of this basal polarity module across the plant body. Top candidates identified here were further tested for their physical interactions with BASL and BRXL2 and examined for their in vivo expression patterns in *Arabidopsis* plants. Among several candidate proteins enriched in the rootward polarity sites, we determined that two AGC kinases play important roles in facilitating hypocotyl upright growth, during which the axes of cell elongation are restricted by cell wall integrity and tightly regulated by the light and gravity vectors.

Results

tSYID-BASL/BRXL2 Reveals Tissue-Wide Polarity in *Arabidopsis* Plants. As described earlier, GFP-BASL driven by the *35S* ubiquitous promoter is broadly expressed and polarized in almost all cells we examined (Fig. 1*A* and *SI Appendix*, Fig. S1 *A* and *B*). In a young seedling (2 d after germination), we observed that the GFP-BASL crescents collectively exhibit a polarity field biased toward the proximal and medial orientations of a developing cotyledon (embryonic leaf) in *Arabidopsis* (Fig. 1*A* and *SI Appendix*, Fig. S1*A*). Below the cotyledon, this tissue-wide polarization pattern transitions into a lateral basal orientation in the hypocotyl (embryonic stem) and becomes predominantly basal in the root (Fig. 1*A* and *SI Appendix*, Fig. S1*B*). For comparison, we generated BRXL2 overexpression lines using the *UBIQUITIN10* (*UBQ10*) promoter. In these plants, BRXL2-mVenus largely recapitulated the basal polarity observed in the hypocotyl and root, but showed more diffuse localization in pavement cells and was preferentially enriched around guard cells (*SI Appendix*, Fig. S1*B*). Together, these results suggest that BASL polarity crescents reflect the presence of a protein network oriented rootward across the plant body.

To identify components of this body-axis basal polarity module, we employed the TurboID-based proximity labeling approach, which has proven particularly powerful in obtaining membrane-localized protein candidates in plants (23). Given the significant accumulation of BASL protein in the nucleus (*SI Appendix*, Fig. S1*B*) with no assigned biological activities (22, 24), we leveraged Split-TurboID, a strategy that emphasizes resolving spatially specific in vivo protein interactomes (20, 25). The principle of Split-TurboID describes that the two halves of the TurboID enzyme can be reconstituted by two physical interactors, thereby restricting the triggered TurboID activity to the interaction location—in our case, the polarity site. Moreover, to assist in visual selection of the reconstituted TurboID in transgenic plants, we integrated YFP expression by developing a tandem fusion of Split-YFP and TurboID (tSYID) system that generates yellow fluorescence upon successful complementation. In this system, BASL was fused with nYFP and cTurboID-myc (n, N-terminal half; c, C-terminal half), while its partner BRXL2 was fused with cYFP and nTurboID-HA, both driven by the *35S* promoter (Fig. 1*B*). The split site G78/G79 in TurboID was previously characterized as a high-affinity combination in mammalian cell lines (20, 25).

To test how the tSYID system works in plant cells, we coinfiltrated nYFP-BASL-cTurboID-myc with cYFP-BRXL2-nTurboID-HA for transient expression in the leaf epidermal cells of *Nicotiana benthamiana*. Protein expression generated from the infiltrated constructs was confirmed by western blotting using anti-myc and anti-HA antibodies (Fig. 1 *C* and *D*). While no significant signals were detected in the respective negative controls, we observed reconstituted YFP signals only when both BASL and BRXL2 were present (Fig. 1*C*). To detect the enzymatic activity of Split-TurboID that may associate with recovered YFP fluorescence, we performed western blotting that reveals protein biotinylating in the plant tissues. As expected, the TurboID activity was reconstituted as demonstrated by protein biotinylation when nYFP-BASL-cTurboID-myc and cYFP-BRXL2-nTurboID-HA were coexpressed (*SI Appendix*, Fig. S2*A*). Importantly, the pattern of biotinylated proteins produced by tSYID-BASL/BRXL2 appeared distinct from that of YFP-TurboID, suggesting the effectiveness of tSYID-BASL/BRXL2 in revealing a specific spatial proteome in the plant cells (tSYID-BASL/BRXL2 at the plasma membrane vs. YFP-TurboID spread everywhere in the cells) (*SI Appendix*, Fig. S2 *A* and *D*).

Building on the success of tSYID in the transient assays, we introduced this system into *Arabidopsis* by cotransforming these two constructs into wild-type (WT) Columbia-0 (Col-0) to obtain tSYID-BASL/BRXL2 plants, and T2 (transgenic generation 2) was used for biological assays. First, confocal microscopy revealed that the recovered YFP signals of *35S*::tSYID-BASL/BRXL2 in young seedlings largely mirrored those of *35S*::GFP-BASL, exhibiting a proximal–distal polarity field in the cotyledon and a rootward basal polarity field in hypocotyl and root cells (Fig. 1 *A* and *D*). Notably, unlike GFP-BASL, tSYID-BASL/BRXL2 showed no nuclear signal in plants (Fig. 1 *A* and *D* and *SI Appendix*, Fig. S1), underscoring the ability of tSYID to resolve the proteome in a specific subcellular location. Next, results from western blotting using Streptavidin-HRP confirmed the success of Split-TurboID enzymatic activity that produced a unique protein-biotinylation pattern for *Arabidopsis* seedlings expressing *35S*::tSYID-BASL/BRXL2 when compared to those produced in the WT plants and transgenic plants expressing *35S*::YFP-TurboID (*SI Appendix*, Fig. S2*B*).

Profiling of the Tissue-Wide Polarity Complex Using Proximity Labeling Proteomics. Next, we proceeded with proximity labeling coupled with mass spectrometry (PL-MS) to identify local protein

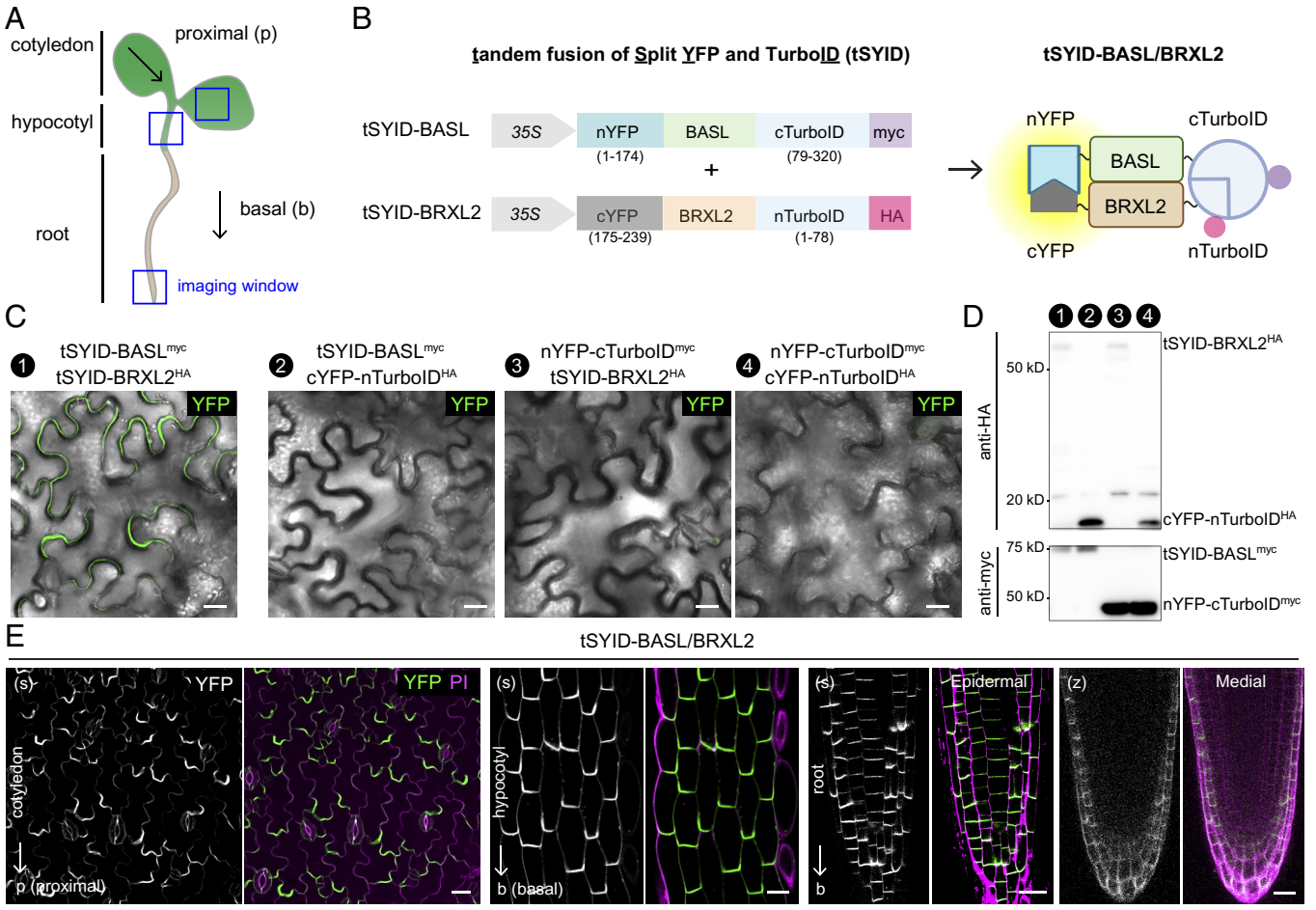

Fig. 1. Design and expression of the tSYID system using interacting BASL and BRXL2 in *Arabidopsis*. (*A*) Diagram of an *Arabidopsis* seedling with imaging areas (blue squares) for confocal microscopy in panel *E*. (*B*) Schematic representation of the constructs used for tandem fusion of Split-YFP and TurboID (tSYID). Constructs include *35S*::nYFP-BASL-cTurboID-myc (tSYID-BASL) and *35S*::cYFP-BRXL2-nTurboID-HA (tSYID-BRXL2). Amino acid ranges for each split protein component are indicated. (*C*) BiFC assay results displayed in *N. benthamiana* leaf epidermal cells. The assay demonstrates interaction between tSYID-BASL and tSYID-BRXL2, with no interaction observed when tSYID-BASL or tSYID-BRXL2 is paired with the corresponding control constructs (cYFP-nTurboID-HA and nYFP-cTurboID-myc). YFP fluorescence indicates sites of protein–protein interaction. (Scale bar, 20 μm.) (*D*) Immunoblot analysis of leaf extracts from the BiFC assay. HA- and myc-tagged tSYID fusion proteins were detected using anti-HA and anti-myc antibodies, respectively. Lanes correspond to samples shown in panel *C*. (*E*) Representative confocal microscopy images of tSYID-BASL/BRXL2 expression in the cotyledon, hypocotyl, and root regions of 3-d-old *Arabidopsis* seedlings. (s) and (z) represent single optical section and z-stack projection images, respectively. (Scale bar, 20 μm.) Arrows indicate the polarity orientation.

components of the BASL/BRXL2 polarity module (Fig. 2*A*). Since PL-MS allows for the identification of both directly and indirectly bound proteins, stringent controls are essential. Here, we employed two controls: WT plants to account for general background signals (nonspecific binding and endogenously biotinylated proteins) and plants expressing cytoplasmic/nuclear YFP-TurboID driven by the ubiquitous *35S* promoter as a nonpolar control (*SI Appendix*, Fig. S2 *C* and *D*). Additionally, we included transgenic plants expressing *35S* promoter-driven LTI6B, a small membrane protein (26), coupled with TurboID-mVenus, as a reference for the plasma-membrane enriched proteomes (*SI Appendix*, Fig. S2 *C* and *D*). Two biological replicates from each sample were conducted for label-free quantitative MS assays (27). Each biological replicate included two technical replicates that were pooled together for protein extraction but underwent independent processing steps, including biotin removal, streptavidin enrichment, on-beads digestion, and liquid chromatography–tandem mass spectrometry (LC-MS/MS). Results from the two MS experiments (MS5931 and MS6226) were processed with Proteome Discoverer (PD) (28) and MaxQuant (MQ) (29) for MS1-based quantification. Through ratiometric analysis (P-value < 0.05 and $\log_2$LFQ > 1, LFQ for Label-Free Quantification), we obtained 196 candidate genes from these two independent experiments, and they were plotted as a Venn diagram (Fig. 2 *B* and *C*). This design—two biological replicates processed by both PD and MQ—was intended to balance both reproducibility and sensitivity in proximity labeling experiments, so that low-abundance or transient interactions can be identified.

To prioritize the candidacy of these 196 genes, we obtained their peptide–spectrum match (PSM) scores and applied filters and obtained 49 high-ranking candidates that were further ordered by Confidence Index [CI] (Fig. 2*D*, details described in *Materials and Methods*). The CI ranking, interestingly, enlists several known interactors of BASL and BRX family proteins to the top, including BSL1/BSL2/BSL3 and D6PK/D6PKL2 (12, 30). These Kelch-repeat BSL protein phosphatases are components of the stomatal polarity module in *Arabidopsis* regulating stomatal fate specification (31). The D6PK proteins, a group of AGCVIII kinases, are predominantly localized to the basal side of plasma membranes in polar cells, such as those in the root tip and vasculature (32). D6PK kinases phosphorylate and activate PIN-FORMED (PIN) auxin transporters, enhancing their ability to transport auxin (33). Importantly, candidates with high CI scores were mainly clustered to the highly overlapping areas in the Venn diagram (Fig. 2*C* and Dataset S1), indicating that there is a high likelihood of using the tSYID system to identify

components associated with the BASL/BRXL2 polarity module at the cell cortex. Not surprisingly, a large portion of these 49 candidates were also detected by the plasma membrane-enriched LTI6B-TurboID-mVenus (*SI Appendix*, Fig. S3*A*).

To compare conventional BRXL2-TurboID proximal labeling with the Split-TurboID-based tSYID-BASL/BRXL2 used in this study, we reanalyzed published BRXL2-miniTurbo (mTb) proteomics data (34). BRXL2 is highly expressed in stomatal lineage cells and exhibits basal polarity in the hypocotyl and root (35). Using two control combinations—OPL2-mTb (a polarity protein with an opposing localization to BRXL2) with WT, and RCI2A-mTb (a plasma membrane-localized protein) with WT—we identified a subset of proteins significantly enriched in BRXL2-mTb samples. Notably, although BRXL2-mTb yielded a smaller number of candidate proteins (16 and 13 in the two respective comparisons), approximately one-third of these were also identified in tSYID-BASL/BRXL2 proteomics (*SI Appendix*, Fig. S3 *B* and *C* and Dataset S2). The overlap between these datasets, along with the additional interactors uniquely identified by tSYID-BASL/BRXL2, provides a strong foundation for investigating the biological relevance of body-axis polarity in plant development and growth.

We further evaluated the biological relevance of the 49 candidate genes through Gene Ontology (GO) analysis (Fig. 2*E*). In the Cellular Component category, "Basal plasma membrane" and "Cell surface" were highly enriched, aligning well with the localization of tSYID-BASL/BRXL2 in plants. Under Molecular Function and Biological Process classification, "Protein serine/threonine kinase activity," "Membrane raft localization," "Phototropism," and "Protein phosphorylation" were highly enriched, indicating cell signaling components and membrane organization likely contribute to the formation and/or functions of the BASL/BRXL2 polarity domain. Interestingly, "Basipetal auxin transport" and "Organelle localization" were also revealed for enrichment, hinting for their functional connection with the tissue-wide BASL/BRXL2 polarity complex (Fig. 2*E*). Moreover, we performed Markov clustering using known protein–protein interactions from the STRING database. The resulting clustered networks were found to closely associate with the identified GO categories, such as "Clathrin-mediated endocytosis," "Exocytosis," "Phototropism," "Membrane raft localization," "Lipid binding," and "Brassinosteroid mediated signaling pathway," revealing the characteristics and potential functions of the BASL/BRXL2 polarity complex (Fig. 2*F*). Representative members in these clusters include DRP1E [a Dynamin-related protein functioning in endocytosis (36)], Sec10/15B [components of the Exocyst complex (37, 38)], PHOT1 [the blue-light photoreceptor mediating phototropic and other responses (39, 40)], D6PKL2 [an AGCVIII kinase that regulates cell-to-cell transport of auxin (33)], REM1.2/1.3 [Remorins that associate with membrane nanodomains, contributing to cell signaling (41)], PATL1/2 [PATELLINs, phospholipid-binding membrane proteins involved in membrane trafficking (42, 43)], and AKR2A/2B [Ankyrin repeat-containing proteins, molecular chaperones for the chloroplast outer envelope proteins (44, 45)], and other uncharacterized proteins.

Subcellular Localization and Expression Pattern of the Candidate Proteins. As signaling molecules and cellular events required for plant growth and adaptation in the changing environment were most intriguing for us, protein candidates in the clusters of "Phototropism," "Brassinosteroid mediated signaling pathway," "Membrane raft localization," and "Lipid binding" were selected for the Split-YFP assay to assess their physical association with either BASL or BRXL2 in *N. benthamiana* leaf epidermal cells. Successful clones for these protein candidates were further examined for their subcellular localization driven by the native promoter for expression in the *Arabidopsis* organs (Fig. 3*B* and *SI Appendix*, Fig. S5*A*).

First, results of the Split-YFP assays in *N. benthamiana* disclosed that most, if not all, of the protein candidates under investigation (9 of them) showed interaction with either BASL or BRXL2 or both. In contrast, the nuclear envelope protein SUN1, used as a negative control, showed no interactions (Fig. 3*A* and *SI Appendix*, Fig. S4). Importantly, all the interactions were detected in the cytoplasm close to the plasma membrane in the leaf epidermal cells, suggesting the high feasibility of our system in identifying components at the BASL–BRXL2 interaction location. Besides several candidates mentioned above (D6PKL2, AKR2A/2B, and REM1.2), we also included SOK3 [a SOSEKI protein that may sense global polarity cue in plant embryogenesis (9, 10)], AGC1-9 [an AGCVIII kinase that may participate in cell wall sensing for root growth (46)], SHOU4L [a novel transmembrane regulator of Cellulose Synthases (47)], and NOI6/7 (proteins with unknown functions). Interestingly, some of the interactions showed polarized patterns in the puzzle-shaped pavement cells in *N. benthamiana*, e.g., AGC1-9 when combined with BASL or BRXL2 (Fig. 3*A*). This behavior is consistent with some of the previously established BASL partners, such as BSL1 and PRAF proteins, when coexpressed with BASL in *N. benthamiana* epidermal cells (30, 48, 49). On the other hand, some showed preferential polarization to a specific cell type, e.g., SOK3 interacts with BASL or BRXL2 around mature guard cells (Fig. 3*A*). However, almost none of these newly identified proteins have been well characterized for their function in plant growth and development.

Next, we examined how these candidate proteins, when fused with mVenus, are expressed in different organs in *Arabidopsis*, with an anticipation that some of the candidates may exhibit polarization patterns resembling those of tSYID-BASL/BRXL2 in the cotyledon, hypocotyl, and/or root. In the leaf epidermis, interestingly, D6PKL2-mVenus was found predominantly expressed in stomatal lineage cells with strong polarization highly mimicking that of BASL or BRXL2 in the native context (Fig. 3*B*) (11, 35). However, mVenus-tagged AKR2A and AKR2B showed notable enrichment in stomatal lineage cells but no polarization observed; they appeared to be broadly expressed and localized to the cytoplasm (Fig. 3*B* and *SI Appendix*, Fig. S5*A*). This observation might be consistent with the previously described localization in the endomembrane reticulum (50). For SOK3-mVenus, as previously reported (9), we observed a consistent protein enrichment at the cell corners (Fig. 3*B*). NOI6-mVenus and REM1.2-mVenus on the other hand exhibited similar localization patterns, ubiquitously distributed near the plasma membrane while no SHOU4L-mVenus signal was detected in the cotyledon (*SI Appendix*, Fig. S5*A*). Thus, among the nine protein candidates we successfully made for in vivo expression, none of them fully replicated the polarization of tSYID-BASL/BRX2 in its proximal–distal field in the cotyledon.

However, when the hypocotyl and root tissues were observed, we identified an intriguing localization pattern of AGC1-9-mVenus that highly resembled tSYID-BASL/BRXL2 in manifesting the apical–basal axis in these tissues (Fig. 3*B*). In contrast, with the exception of SOK3 and D6PKL2 exhibiting polarization in some specific cell types—none of the rest candidates, i.e., AKR2A, AKR2B, SHOU4L, REM1.2, NOI6, and NOI7, were polarized to the basal side of the hypocotyl and root cells (Fig. 3*B* and *SI Appendix*, Fig. S5*A*). Thus, AGC1-9 became our major interest to pursue the biological relevance of body-axis polarity in plant development and growth.

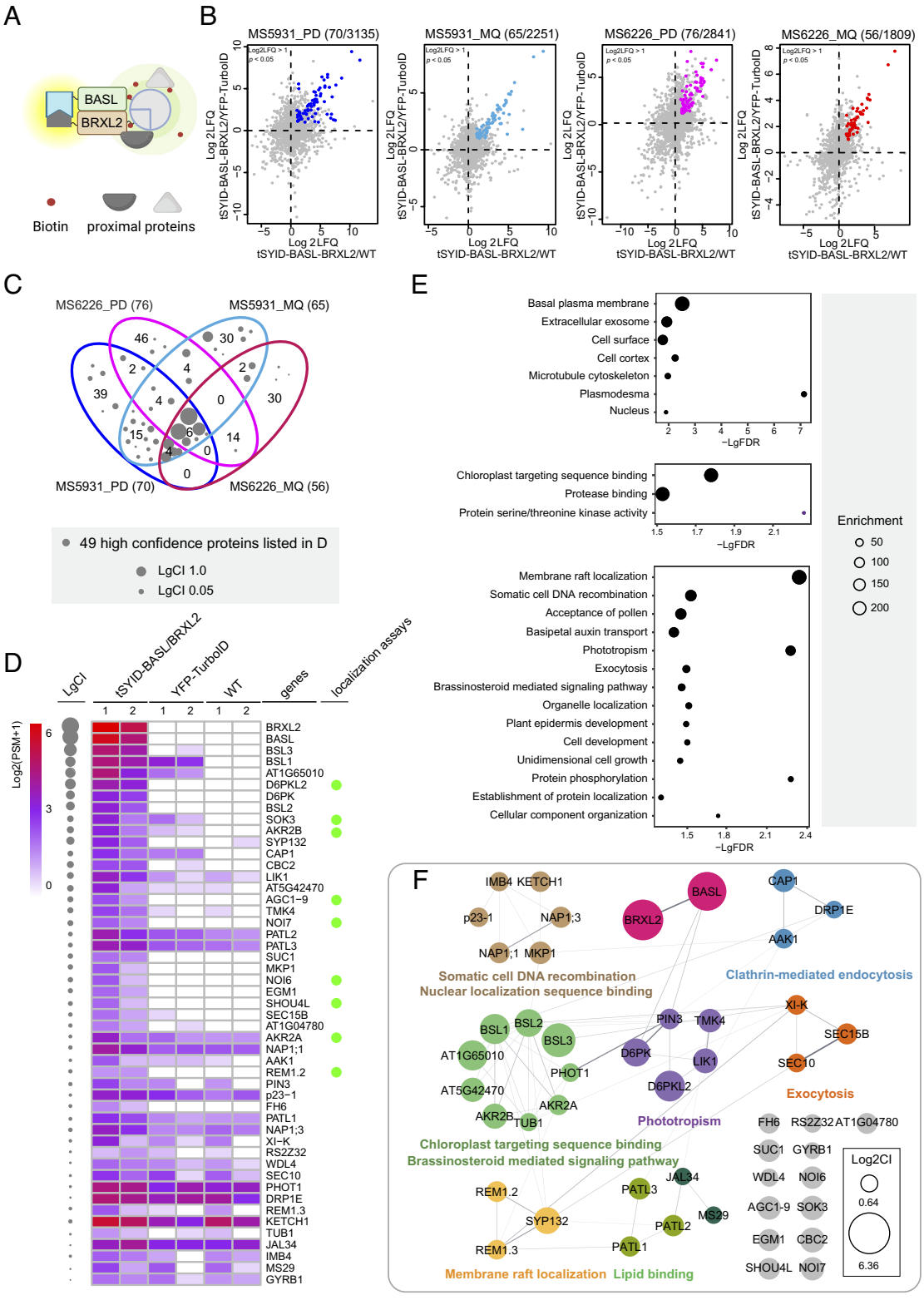

Fig. 2. Proximity proteomics profiling of tSYID-BASL/BRXL2 in *Arabidopsis*. (*A*) Schematic representation of the tSYID-BASL/BRXL2 used for proximity labeling to identify neighboring proteins. (*B*) Ratiometric analysis of proteomic data highlights specific substrates of tSYID-BASL/BRXL2. Biotin labeling was performed on 3-d-old Col-0 and transgenic seedlings expressing tSYID-BASL/BRXL2 or *35S*::YFP-TurboID. Axes represent the log values of LFQ ratio between two samples. tSYID-BASL/BRXL2 enriched candidate proteins were selected based on defined criteria (fold change > 2, $P < 0.05$) compared to both controls. Differently colored dots represent proteins identified above the threshold using either PD or MQ spectral search software. The number of tSYID-BASL/BRXL2 enriched candidates and total proteins identified are indicated above each scatter plot. (*C*) Venn diagram illustrating the overlap and specificity of tSYID-BASL/BRXL2 enriched candidate proteins identified by PD and MQ mass spectrometry analyses. The average protein spectrum matches (avePSM) ratios are used to calculate the confidence index (CI), with node size correlating to the enrichment level (LgCI). (*D*) Heatmap of normalized average PSM values for identified candidates from tSYID-BASL/BRXL2. Inclusion criteria are avePSM of tSYID-BASL/BRXL2 ≥ 1, avePSM ratio of tSYID-BASL/BRXL2 to YFP-TurboID ≥ 1, and avePSM ratio of tSYID-BASL/BRXL2 to WT ≥ 1.5, performed over two biological and two technical replicates. (*E*) GO analysis of the 49 highly enriched proteins categorized into Biological Process, Cellular Components, and Molecular Function based on their FDR. (*F*) Markov clustering of the 49 enriched proteins based on protein–protein interaction scores from the STRING database. Gray lines represent interactions; node size reflects relative enrichment (Log_2CI). Each cluster is annotated with associated GO terms.

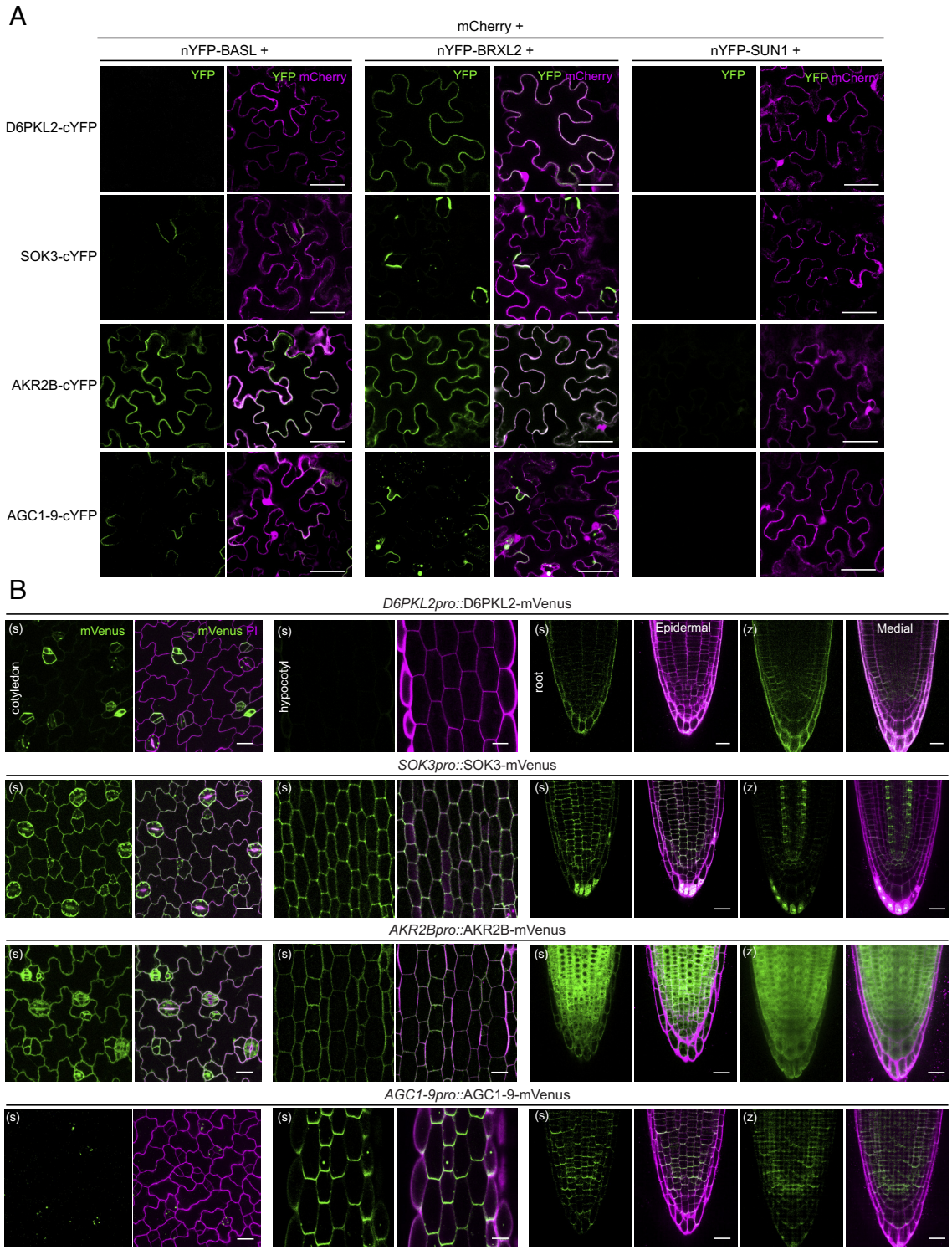

Fig. 3. Validation and localization of candidate proteins from tSYID-BASL/BRXL2 proximity proteomics. (*A*) BiFC assays conducted in *N. benthamiana* leaf epidermal cells to test interactions between BASL/BRXL2 and selected candidate proteins: D6PKL2, SOK3, AKR2B, and AGC1-9. The nuclear envelope protein SUN1 fused to nYFP serves as a negative control. YFP fluorescence indicates protein–protein interactions. Merged images display YFP fluorescence overlaid with mCherry fluorescence for spatial context. (Scale bar, 50 μm.) (*B*) Confocal microscopy images showing the endogenous localization of identified candidate proteins tagged with mVenus in various tissues of 3-d-old *Arabidopsis* seedlings. Candidates shown include D6PKL2, SOK3, AKR2B, and AGC1-9, visualized in the cotyledon, hypocotyl, and root. Images include fluorescence (mVenus) alongside PI staining to outline cell boundaries. (s) and (z) represent single optical section and z-stack projection images, respectively. (Scale bar, 20 μm.)

AGC1-9 Is a Rootward Polarized Protein in the Hypocotyl. AGC1-9 belongs to the AGCVIII kinase subfamily, members of which participate in a diverse range of developmental and cellular processes in plants (46, 51). Previous research showed that KIPK (KCBP-INTERACTING PROTEIN KINASE), a close homolog of AGC1-9 (Fig. 4*A*), interacts with the Proline-rich, Extension-like, Receptor-like Kinases (PERKs) and a Kinesin-like Calmodulin-binding Protein (KCBP) to regulate root growth (46, 52). AGC1-9 was therefore also named KIPKL1 and AGC1-8 named KIPKL2 (53). We examined the expression patterns of KIPK and AGC1-8 by observing the native promoter-driven mVenus-tagged protein expression in vivo. We were not

able to establish how AGC1-8-mVenus is localized because of the failures in obtaining transgenic plants expressing detectable fluorescent signals, but KIPK-mVenus almost replicated AGC1-9-mVenus in its rootward polarization across all cell types in the hypocotyl and root (Figs. 3*B* and 4*B* and *SI Appendix*, Fig. S5*B*). Unlike AGC1-9-mVenus, KIPK-mVenus is also expressed in the cotyledon (Fig. 4*B*).

Given their close relationship on the phylogenetic tree and similar expression patterns in the hypocotyl and root, we hypothesized that these AGC kinase members may play redundant functions in vivo. By using the CRISPR/Cas9-mediated genome editing strategy (54), we generated *agc1-9;kipk* double and *agc1-9;kipk;agc1-8* triple mutants (specific mutations are detailed in *SI Appendix*, Fig. S6). Regarding general plant growth, we found that *agc1-9;kipk* CRISPR-generated mutants showed elongated root growth (*SI Appendix*, Fig. S7 *B* and *D*), consistent with the phenotype observed in the T-DNA insertional mutants (46). Intriguingly, while the double mutants grew largely normally under light conditions, we observed striking phenotypes when these mutants were covered with foil to mimic a dark environment—their hypocotyls failed to grow vertically but formed a wavy and agravitropic growth pattern (Fig. 4*C*). In the WT, the hypocotyls exhibit normal vertical elongation, typical of etiolation, a process that promotes rapid stem elongation and maintains apical dominance to help seedlings reach light. In the *agc1-9;kipk,* while the overall hypocotyl length in the mutants does not appear to change significantly (*SI Appendix*, Fig. S7 *A* and *C*), the inability to sustain vertical elongation underlines a specific defect in directional growth, rather than a general growth impairment. The wavy growth phenotype of *agc1-9;kipk* in the dark was not further enhanced by additional mutations in *AGC1*-8 (Fig. 4 *C* and *D*), thus pointing to a potential role for KIPK and AGC1-9 kinases as primary regulators in the regulation of gravitropic responses or the maintenance of mechanical integrity required for vertical orientation during elongation.

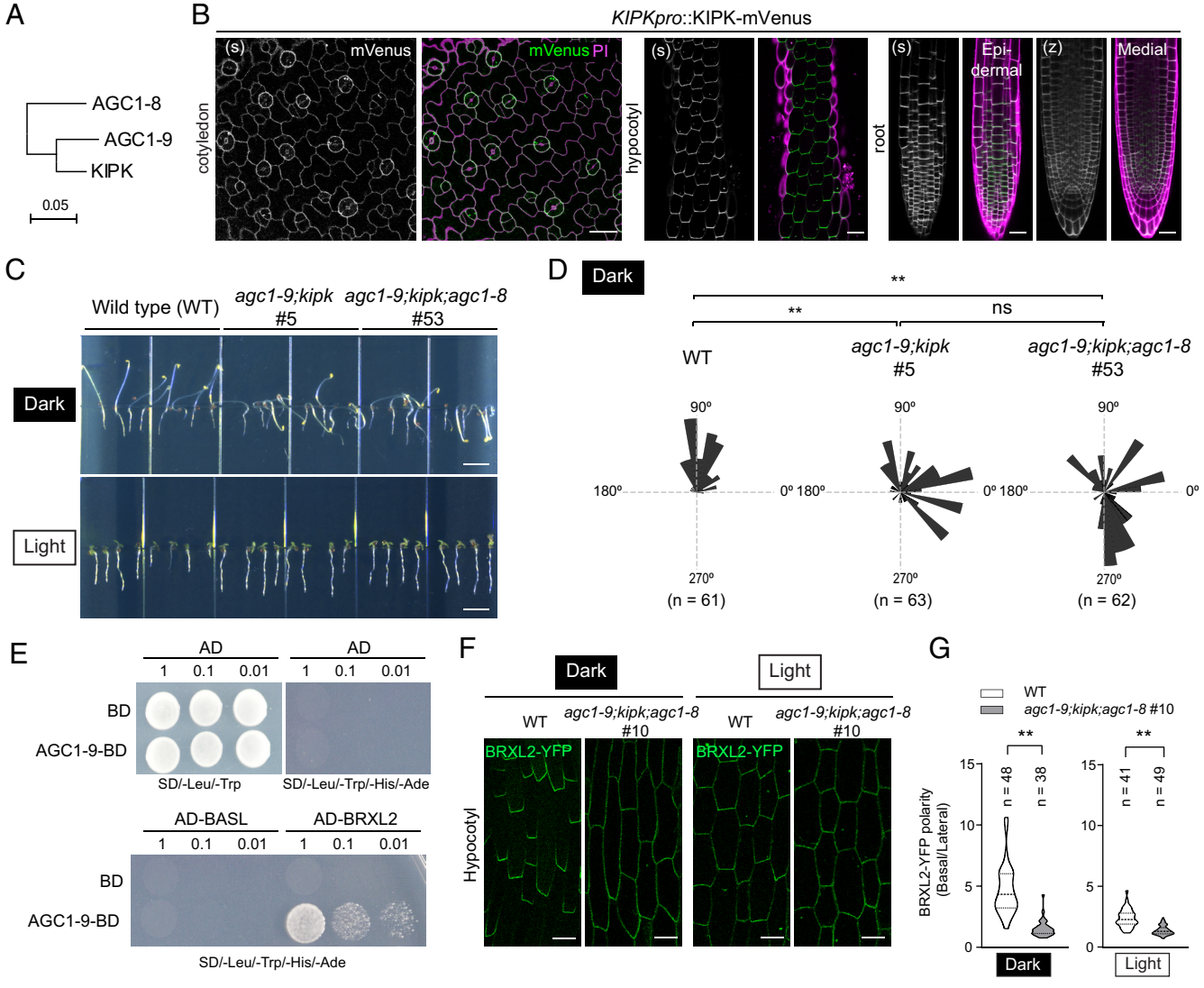

Fig. 4. Functional analysis of AGC1-9 and its close homologs in hypocotyl and root development. (*A*) Phylogenetic tree of AGC1-9 and closely related homologs. (*B*) Confocal microscopy of *KIPKpro*::KIPK-mVenus expression in 5-d-old *Arabidopsis* seedlings. (s) and (z) represent single optical section and z-stack projection images, respectively. (Scale bar, 30 μm.) (*C*) Phenotypic comparison of *agc1-9;kipk* double and *agc1-9;kipk;agc1-8* triple mutants with WT under varying light conditions. "Dark conditions" were simulated by covering the plates with one layer of aluminum foil in the growth chamber. (Scale bar, 5 mm.) (*D*) Statistics of hypocotyl growth orientation in the WT background for *agc1-9;kipk* double and *agc1-9;kipk;agc1-8* triple mutants under dark conditions. (*E*) Yeast two-hybrid assays demonstrate interaction between AGC1-9 and BRXL2 across different dilutions. (*F*) Representative hypocotyl confocal images of BRXL2-YFP in WT and *agc1-9;kipk;agc1-8* mutant background. (Scale bar, 20 μm.) (*G*) Quantitative analysis of BRXL2-YFP polarity in hypocotyl cells. Violin plots illustrate the polarity index of BRXL2-YFP in WT and *agc1-9;kipk;agc1-8* mutant background under both dark and light conditions, with kernel density estimates of data distribution. The central dashed line represents the median, with the upper and lower bounds indicating the first and third quartiles, respectively. Statistical significance is indicated as ** ($P < 0.01$) and ns (nonsignificant). Sample sizes (n) are noted for each group.

Next, we investigated whether the BASL/BRXL2-marked rootward polarity site is affected by the *agc1-9;kipk* mutations in the hypocotyl. Using the yeast two-hybrid assays, we determined that AGC1-9 directly interacts with BRXL2 but not BASL (Fig. 4*E*). Thus, we leveraged the strong expression and polarization of BRXL2-YFP in the hypocotyl to assess the cellular defects of *agc1-9;kipk;agc1-8* mutants. Under light and dark conditions, the expression pattern of BRXL2-YFP driven by its own promoter recapitulated the strong rootward enrichment of AGC1-9-mVenus or KIPK-mVenus in the hypocotyl (Fig. 4*F*). In the absence of *AGC1*-9, *KIPK*, and *AGC1-8,* the dark-grown seedlings exhibit wavy hypocotyl growth, yet this does not affect the hypocotyl length, as observed in Col-0 background (*SI Appendix*, Fig. S7 *E–G*). Interestingly, we found BRXL2's polarization became less pronounced in both dark and light conditions in the mutants (Fig. 4 *F* and *G*, measured as Polarity Index as described in *SI Appendix*, Fig. S7*G*), suggesting that these AGC kinases play a role in enforcing BRXL2 rootward polarity in the hypocotyl. Furthermore, it is worth noting that BRXL2-YFP was more strongly polarized in the dark than it was in the light (Fig. 4*F*), indicating that this basal polarity module is light sensitive and likely contributes to the fast and robust hypocotyl growth in the dark. The wavy hypocotyl growth observed for *agc1-9;kipk* or *agc1-9;kipk;agc1-8* mutants grown in the dark might be partially caused by compromised BRXL2 polarization.

Discussion

tSYID: Proximity Labeling of Interacting Polarity Proteins. In stomatal lineage cells, several scaffold proteins, including BASL, the BRX family (35), and the POLAR proteins (55), have been identified as key components of the polarity complex. These proteins exhibit differential distributions and dynamic behaviors during development (56, 57), which pose challenges for traditional full-length TurboID fusions that often lack specificity in capturing shared polarity partners. In this study, we successfully implemented the contact-based Split-TurboID system (tSYID) in plants. This system offers advantages in spatially and temporally controlled biotinylation activity (25). Our tSYID approach is further enhanced by the ease of selecting recombined TurboID through the visual detection of reconstituted YFP fluorescence in planta (Fig. 1*B*). This visual confirmation provides a straightforward and efficient method to verify system functionality. By capturing transient interactions, operating in vivo, and preserving the spatial and temporal contexts of protein interactions, the tSYID system represents an excellent tool for studying the interactome of polarity proteins in plants.

While after a few failed attempts in generating a fully comparable BRXL2-TurboID line, we found that proximity labeling using miniTurbo-tagged BRXL2 has been employed to profile the interactomes of this polarity protein in *Arabidopsis* stomatal lineage cells (58). Opposing the BRX-BASL-POLAR polarity domain is the domain marked by the polarization of OCTOPUS-LIKE (OPL) proteins, particularly OPL2 (59). It was shown that, in stomatal lineage cells, D6PKL2 associates with the BASL/BRXL2 site, whereas SOK3 associates with the OPL2 site (58). However, using the broadly expressed tSYID-BASL/BRXL2, we not only identified D6PKL2 but also SOK3 to likely act as a proximal partner (Fig. 3). Given the broad expression of SOK3 across the plant body, it is likely that SOK3 acts as a central hub for the assembly of cell polarity complexes in many cell types, consistent with previous reports (58). Whether and how some of these processes could be achieved by the D6PKL2-mediated activities remains unknown, but it was shown that YFP-D6PK is basally polarized in root epidermis, promotes PIN-mediated auxin transport (33), and contributes to hypocotyl phototropism in *Arabidopsis* (60). Given that D6PK is one of the highest confidence genes we identified as potentially associated with tSYID-BASL/BRXL2, we hypothesized that the tSYID-BASL/BRXL2 basal polarity site may play important roles in plant development and responses to environmental stimuli (61, 62).

Functions of the Apical and Basal Polarity Proteins in Plants. Opposing polarity domains have been identified in both plants and animals to play critical roles in directing cellular asymmetry, cell division, and development (63, 64). For example, in *Drosophila* neuroblast asymmetric cell division (ACD), the apical Par complex is antagonized by the Scribble complex that ensures basal polarity (65). Distinct molecular components associated with the opposing polarity domains guide spindle orientation and ensure the asymmetric segregation of cell fate determinants (66, 67). Developing stomatal lineage cells that undergo ACD also possess opposing polarity domains in both dicot and monocot plants, i.e., the BASL-POLAR-BRX vs. OPL2 domains in *Arabidopsis* and the ZmPAN1-PAN2-BRK1 vs. BdPOLAR domains in maize and *Brachypodium* (34, 68, 69). Functions of these polarity complexes have been connected to cell-fate specification (22), dynamic cytoskeleton organization (68, 70), and nuclear migration (71).

Beyond the stomatal lineage, oppositive polarity domains were identified to link cell fate determination. Specifically, BRX is polarized at the rootward plasma membrane in developing protophloem, where it inhibits the activity of PROTEIN KINASE ASSOCIATED WITH BRX (PAX) in auxin efflux at low auxin levels, thus acting as a rheostat to maintain auxin homeostasis required for protophloem differentiation (12). In the same developing protophloem cells, the OCTOPUS (OPS) scaffold protein, opposing to the BRX domain, is associated with the shootward plasma membrane (72). OPS may function through antagonizing the BIN2 kinase to promote phloem differentiation in plants (73). In the hypocotyl and root apical–basal polarity system, although we did not identify BIN2 to associate with the tSYID-BASL/BRX complex, we do not rule out possible functional contributions of BIN2 in hypocotyl elongation. It is well established that BIN2 negatively regulates hypocotyl growth by inhibiting the BR signaling pathway and integrating environmental and hormonal cues (74–77). A recent work using TurboID-based proximity labeling mapped the BIN2 signaling network and disclosed protein candidates functioning in phototropism, vesicle trafficking, and cytoskeleton organization, suggesting that these processes are likely regulated by BIN2 activities (78). Components of these processes were also identified in our study (Fig. 2*F*), and their functions should be investigated for possible connection with the basal protein complex and regulation of hypocotyl growth.

Potential Roles of BRXL2–BASL Network Components in Basal Side Polarity. The proximity labeling network centered on the BRXL2–BASL interaction reveals an interconnected group of proteins that likely contribute to the establishment and maintenance of tissue-wide polarity in *Arabidopsis*. The identification of AGC kinases—including AGC1-9, D6PK, and D6PKL2—alongside the blue-light receptor kinase PHOT1 and the auxin transporter PIN3, points to a regulatory axis linking polarity with directional auxin transport. Some of these kinases are known for their roles in phosphorylating PIN proteins to modulate their localization and activity (32, 53, 79–81), and their enrichment in this network supports the hypothesis that BRXL2 may scaffold AGC kinases to spatially control auxin efflux in support of growth responses such as phototropism and gravitropism.

Further supporting this model, several key components of membrane trafficking and vesicle transport machinery were identified, including KETCH1, SYP132, SEC10, SEC15B, p23-1, and CAP1. These proteins are essential for targeted delivery and recycling of polarity regulators and cargo proteins to the plasma membrane (82–86). Their presence suggests that dynamic membrane trafficking might be needed for reinforcing the BRXL2–BASL polarity domain at the plasma membrane. It is also possible that their engagement may contribute to local cell expansion, a process promoted by BASL accumulation (11). In parallel, the identification of cytoskeletal regulators such as WDL4, TUB1, and FH6 highlights possible involvement of microtubule and actin networks in stabilizing polarity domains and facilitating the spatial distribution of vesicles and protein complexes (87–90). Lipid signaling components, including PATL1–3 and LIK1 (91, 92), as well as the presence of REMORIN proteins REM1.2 and REM1.3, markers of membrane nanodomains (93, 94), further supports a model in which BRXL2–BASL operates within specialized plasma membrane subregions that facilitate precise spatial signaling. Taken together, these candidate interactors support the view that the BRXL2–BASL complex functions as a central integrator of signaling, trafficking, and structural pathways, coordinating asymmetric protein localization and directional development across multiple tissue layers in *Arabidopsis*.

Possible Functions of AGC1-9 and KIPK Proteins. Interestingly, we observed that the AGC protein kinases, AGC1-9 and KIPK, exhibited strong rootward polarized localization in the hypocotyl and root cells (Figs. 3*B* and 4*B* and *SI Appendix*, Fig. S5*B*). Consistent with the previous report (95), knocking out AGC1-9 and KIPK resulted in longer roots in *Arabidopsis* (*SI Appendix*, Fig. S7 *B* and *D*). It was also shown that AGC1-9 and KIPK may associate with PERK receptor-like kinases, which contain an extracellular extensin-like domain likely functioning as wall-associated kinases (WAKs) to monitor changes in the cell wall during plant cell expansion (96). Furthermore, AGC1-9 and KIPK also interact with KCBP, a kinesin-like motor protein involved in trichome morphogenesis and root growth (97, 98). This kinesin-14 KCBP binds to the microtubule and was known to be regulated by calmodulin (CaM) in the presence of Ca^{2+} (46). Given the enrichment of KIPK along the plasma membrane, it is plausible that the PERK-KIPK-KCBP module forms a signaling continuum across the cell wall, plasma membrane, and microtubule cytoskeleton to negatively regulate cell elongation during root development in *Arabidopsis*.

Besides root growth, the most striking phenotype of *agc1-9;kipk* mutants was observed in the hypocotyl, where growth orientations appeared random (Fig. 4 *C* and *D*), partly reflecting their disturbed gravitropic responses. Recently, Xiao et al. reported the roles of KIPK and KIPKL1/AGC1-9 in suppressing hypocotyl overbending during negative gravitropic growth in *Arabidopsis* (53, 99). It was found that KIPK phosphorylates PIN3, BRXL2, and ARMODILLO REPEAT KINESIN (ARK) proteins, which likely regulate auxin transport and cortical microtubule network, respectively, to facilitate hypocotyl penetration through the soil, a process integrating plant's obstacle voidance and negative gravitropic growth (53). Xiao's work further highlighted a synergistic role of KIPK, KIPKL1/AGC1-9, and NEK6 (NIMA-RELATED PROTEIN KINASE 6) in regulating ARK proteins, proposing a working model in which these AGCVIII kinases coordinate cortical microtubule organization to support efficient hypocotyl bending (53).

On the other hand, our work demonstrated that AGC1-9 and KIPK are central players for the hypocotyl to grow straight in the dark but not in the light (Fig. 4 and *SI Appendix*, Fig. S7), suggesting signaling crosstalk between light conditions and gravitropic and/or cell wall–integrated growth in plants. Light and gravity are two key environmental factors that coordinately regulate plant growth. In this process, phytochrome B (phyB) appears to act as a key link between light perception and plant gravitropism (100). When a plant is exposed to red light, phyB is activated to induce protein degradation of the four phytochrome-interacting factors (PIFs) that promote amyloplast development (100). The sedimentation of starch-containing amyloplasts in gravity-sensing cells could trigger signaling cascade to redirect auxin transportation causing the plant organ to bend in the right direction (101). More recently, PIFs' function in hypocotyl growth has been linked to the expression of LAZY4, one key factor functioning in gravitropism in several plant species (102). While the entire molecular mechanisms is not resolved, the LAZY proteins are thought to link gravity sensing to the altered auxin transport in the root, in part through protein repolarization at the plasma membrane (103). The mutant phenotype we observed, the wavy hypocotyl growth of *agc1-9;kipk* in the dark, revealed the functional relevance of these kinases in coordinating hypocotyl skotomorphogenesis and negative gravitropic growth. Whether AGC1-9 and KIPK function with phyB, PIFs, or LAZYs to regulate hypocotyl growth in different light conditions needs to be further investigated.

It is important to note that we observed that the rootward polarization of BRXL2 in the hypocotyl was greatly reduced in the *agc1-9;kipk;agc1-8* triple mutants (Fig. 4 *F* and *G*). Previous work has established that BRX and the AGC kinase PAX fine-tune auxin efflux by modulating PIN activity, thereby orchestrating root protophloem differentiation (12). The polarity of BRX depends in part on its interaction with PAX, and this partnership is stabilized through the recruitment of PIP5K enzymes that modulate phosphoinositide balance at the membrane (104). In our study, although the exact molecular partners of AGC1-9 remain to be identified, its function appears to mirror aspects of the BRX–PAX module: influencing polarity at the basal side of cells and affecting tropic growth responses. This suggests that AGC1-9 might similarly act through a polarity-stabilizing mechanism, possibly involving BRXL2 and downstream components analogous to PINs. Thus, we propose that the robust polarization of hypocotyl cells, revealed by BRXL2 localization, could be a part of the cellular machinery required for hypocotyl upright growth, a complex trait controlled by both extrinsic and intrinsic signals (105).

Materials and Methods

Plant Growth Conditions. *Arabidopsis* (*Arabidopsis thaliana*, Columbia ecotype) seeds were surface sterilized with 70% ethanol for 1 min and 20% (v/v) bleach for 8 min and rinsed with sterile water for five times before planted on the ½ Murashige and Skoog (½ MS) medium supplied with 0.7% agar. After 2 d of stratification at 4 °C, plants were moved to the plant growth chamber and grown under a photoperiod of 16 h-light and 8 h-dark at 22 °C. For proximity labeling and mass spectrometry, 3-d-old seedlings were used. *N. benthamiana* plants used for transient protein expression were grown under the same conditions except that the seeds were planted directly into the soil.

Vector Construction. tSYID-BASL/BRXL2 cloning was performed using a multisite gateway system. First, cYFP and nYFP, which split from EYFP, were cloned into the multisite gateway entry vector pBSDONR p1-p4 using BP reaction (BP clonase™ II, Thermo Fisher, Cat#11789020). BASL and BRXL2 were cloned into

pBSDONR p4r-p2. Second, nTurboID-HA and cTurboID-myc were incorporated into pEarleyGate100 and engineered pEarleyGate100 with Hygromycin resistance (termed pHygGate100), respectively, through DNA assembly. The tSYID-BASL construct was generated by fusing nYFP_pBSDONR_L1-L4 and BASL_pBSDONR_R4-L2 into the destination vector nTurboID-HA_pEarleyGate100 by LR reaction (LR clonase™ II plus, Thermo Fisher, Cat#12538200). Similarly, the tSYID-BRXL2 construct was generated by fusing cYFP_pBSDONR_L1-L4 and BRXL2_ pBSDONR_R4-L2 into the destination vector cTurboID-myc_pHygGate100. For constructs used in the bimolecularfluorescence complementation (BiFC) assays, nYFP-BASL, nYFP-BRXL2, and nYFP-SUN1 were generated by fusing nYFP_pBSDONR_L1-L4 and BASL/BRXL2/SUN1_pBSDONR_R4-L2 into the destination vector pEarleyGate100 by LR reaction. The cYFP constructs were generated by fusing the genomic sequences of target genes into an engineered cYFP-pYBA1132 construct through DNA assembly. For constructs used for observing protein localization, the promoter and genomic sequences of target genes were cloned into pENTR/D-TOPO through NotI and AscI sites. The pENTR constructs were recombined into pGWB501-based TurboID-mVenus destination vector through LR reaction.

To create CRISPR/Cas9-mediated mutagenesis in *Arabidopsis*, we adopted the system described in a previous study (106). The single guide RNA (sgRNA) sequences that target AGC1-9, KIPK, and AGC1-8 were designed using the webserver CRISPOR (http://crispor.tefor.net/). Using pCBC-DT1T2 as the template, the sgRNA1 (AGC1-9)-U6-26t-U6-29p-sgRNA2 (AGC1-9), sgRNA1 (KIPK)-U6-26t-U6-29p-sgRNA2 (KIPK), sgRNA1 (AGC1-8)-U6-26t-U6-29p-sgRNA2 (AGC1-8) and sgRNA3 (AGC1-9)-U6-26t-U6-29p-sgRNA3 (KIPK) cassettes were amplified by PCR and inserted into engineered pHEE401 with BASTA resistance (pBEE401) by GoldenGate assembly to obtain pBEE401-AGC1-9_sgRNA12, pBEE401-KIPK_sgRNA12, pBEE401-AGC1-8_sgRNA12, pBEE401-AGC1-9_sgRNA3-KIPK_sgRNA3. Then U6-26p- sgRNA1 (KIPK)-U6-26t-U6-29p-sgRNA2 (KIPK)-U6-26t was amplified from pBEE401-KIPK_sgRNA12 and incorporated into pBEE401-AGC1-9_sgRNA12 through DNA assembly at Nco I restriction enzyme site to obtain pBEE401-AGC1-9_sgRNA12_KIPK_sgRNA12. Similarly, the U6-26p-sgRNA1 (AGC1-8)-U6-26t-U6-29p-sgRNA2 (AGC1-8)-U6-26t and U6-26p-sgRNA3 (AGC1-9)-U6-26t-U6-29p-sgRNA3 (KIPK)-U6-26t fragments were sequentially incorporated into pBEE401-AGC1-9_sgRNA12_KIPK_sgRNA12 via DNA assembly to generate the final construct, pBEE401-AGC1-9_sgRNA123_KIPK_sgRNA123_AGC1-8_sgRNA12.

The plasmids were transformed into Agrobacterium tumefaciens GV3101, which were used for stable transformation in *Arabidopsis* and transient expression in *N. benthamiana*. *Arabidopsis* plants were transformed with the standard floral dipping method, and the T0 seeds were subjected to antibiotic selection.

Split-TurboID Verification In Planta. Split-TurboID verification experiments were conducted by transiently expressing proteins in *N. benthamiana* leaves. These leaves were infiltrated with *Agrobacterium* carrying the appropriate constructs as described above. We collected the leaves 48 h after infiltration to extract proteins using a buffer composed of 50 mM Tris-HCl (pH 7.5), 150 mM NaCl, 0.5% NP-40 (v/v), 0.5% Triton X-100 (v/v), 0.5% sodium deoxycholate (w/v), 40 μM MG132, and 1× Protease Inhibitor Cocktail. After centrifugation at 13,000 rpm and 4 °C for 10 min, the supernatant was collected. The protein samples were then boiled with loading buffer and subjected to SDS–PAGE separation. For western blot analysis, we used streptavidin-HRP (Abcam, #7403, 1:10,000), anti-GFP (Roche, 11814460001, 1:2,000), anti-myc (Cell Signaling Technology, 9B11, 1:1,000), and anti-HA antibodies (Sigma, H9658, 1:2,000).

Proximity Labeling and Free Biotin Depletion. For proximity labeling, 3-d-old transgenic seedlings expressing protein tagged with reconstituted TurboID were submerged in 50 μM biotin solution for 30 min at room temperature before being washed three times with water and harvested. Total protein was extracted by grinding the sample with extraction buffer [50 mM Tris-HCl (pH 7.5), 150 mM NaCl, 0.5% NP40 (v/v), 0.5% Triton X-100 (v/v), 0.5% sodium deoxycholate (w/v), 40 μM MG132, 1× Protease Inhibitor Cocktail]. The supernatant was collected after samples were centrifuged at 13,000 rpm at 4 °C for 10 min.

For desalting chromatography, the ÄKTA protein purification system (GE Healthcare) with 3 × 5 mL HiTrap desalting columns (GE Healthcare, Cat#GE29-0486-84) was utilized. About 2 mL of total proteins for each sample was loaded into the HiTrap column after equilibration with desalting buffer (50 mM Tris-HCl pH 7.5, 0.05% Triton X-100) using a 5 mL syringe with a 2 mL sample loop. The flow rate used for all experiments was 0.7 mL/min with 0.5 Mpa as the pressure limit. The salt eluates containing free biotin with high conductivity were abandoned while the total protein elutes with UV280 absorbance peak were collected for affinity purification (AP).

Affinity Purification by Streptavidin-Coated Beads. Approximately 4 mL of desalted protein eluate was collected for each sample and mixed with 100 μL of streptavidin-coated magnetic beads (Dynabeads™ MyOne™ Streptavidin C1, Thermo Fisher, 65002) for affinity purification. After overnight incubation with rotation at 4 °C, the beads were separated using a magnetic rack and washed five times with extraction buffer. Five percent of the beads were harvested, and the proteins were eluted by boiling at 98 °C for 10 min in 1× SDS loading buffer before separation by SDS-PAGE. The remaining beads were washed four times with 1× PBS to remove detergent prior to trypsin digestion.

On-Beads Digestion. 0.2 μg of trypsin in 20 μL of 50 mM NH_4HCO_3 was added to the washed and ready-to-digest beads, followed by incubation at 37 °C for 4 h. An additional 0.2 μg of trypsin was added, and the mixture was incubated overnight at 37 °C. The solution was then separated from the beads, and the pH was adjusted to 3 using 10% formic acid. The sample was desalted using a stage tip prior to LC-MS/MS analysis.

LC-MS/MS. Samples were analyzed using a Nano LC-MS/MS system (Dionex Ultimate 3000 RSLCnano) interfaced with an Orbitrap Eclipse Tribrid mass spectrometer (Thermo Fisher Scientific). Samples were loaded onto a fused silica trap column (Acclaim PepMap 100, 75 μm × 2 cm, Thermo Fisher Scientific). After a 5-min wash at 5 μL/min with 0.1% TFA, the trap column was aligned with an analytical column (Nanoease MZ Peptide BEH C18, 130 Å, 1.7 μm, 75 μm × 250 mm, Waters). Peptides were eluted at 300 nL/min using a segmented linear gradient of 4 to 15% solvent B over 30 min, 15 to 25% B over 40 min, 25 to 50% B over 44 min, and 50 to 90% B over 11 min, followed by a re-equilibration to 4% B for 5 min for subsequent runs. Solvent A was 0.2% formic acid, and solvent B was 0.16% formic acid in 80% acetonitrile.

The scanning sequence began with an MS1 spectrum (Orbitrap analysis, resolution 120,000, scan range from m/z 350 to 1,600, automatic gain control (AGC) target 1E6, maximum injection time 100 ms). Parent ions were selected based on the top S (3 s) and a dynamic exclusion of 60 s. Parent masses were isolated in the quadrupole with a 1.4 m/z isolation window, AGC target 1E5, and fragmented using higher-energy collisional dissociation with a normalized collision energy of 30%. The fragments were scanned in the Orbitrap with a resolution of 30,000. The MS/MS scan range varied depending on the charge state of the parent ion, with a minimum mass limit set at 100 amu.

Database Search and Analysis. LC-MS/MS data were analyzed with Proteome Discoverer 3.0 (Thermo Fisher Scientific) using the Sequest HT search engine against the TIAR 11 proteome database (Araport11_genes_201606.Pep.fasta) and a database of common lab contaminants. Trypsin was set as the protease, allowing up to 2 missed cleavages. The MS mass tolerance was set at ±10 ppm and MS/MS mass tolerance at ±0.02 Da. Dynamic modifications included methionine oxidation, phosphorylation on serine, threonine, or tyrosine, protein N-terminal acetylation, and N-terminal methionine loss (with or without acetylation). Percolator was used for result validation, employing a concatenated reverse database for a target-decoy strategy. Phosphosite confidence was calculated using phosphoRS. High confidence for proteins and peptides was defined as FDR < 0.01 and medium confidence as FDR < 0.05. Peak intensities were used for precursor abundance measurement.

Additionally, MaxQuant version 2.4.9.0 with the Andromeda search engine was employed for analysis against the same proteome database and contaminant database. The same settings for trypsin and variable modifications were used. Protein and peptide false discovery rates (FDR) were set at 1%. Only proteins not identified solely by modified sites were considered valid, with reverse hits and common contaminants removed. MaxLFQ was used for protein quantification.

For data analysis, we applied the DEP package in R software and performed ratiometric analysis to enrich candidates using at least two controls. The complete LFQ data are provided as Dataset S3, and the detailed R scripts for candidate enrichment analysis are as below:

```
library("dplyr")
library("DEP")
library(SummarizedExperiment)
data<-read.csv("MS6226-MS5931_PD data/MQ data.
  csv,"stringsAsFactors=FALSE)
des<-read.csv("Design.csv",stringsAsFactors=FALSE)
data_unique <- make_unique(data, "Gene.names," "Protein.
  IDs," delim=";")
LFQ_columns <- grep("LFQ.", colnames(data_unique))
data_se <- make_se(data_unique, LFQ_columns, des)
plot_frequency(data_se)
data_filt2 <- filter_missval(data_se, thr = 1)
plot_frequency(data_filt2)
data_norm <- normalize_vsn(data_filt2)
plot_normalization(data_filt2, data_norm)
data_imp <- impute(data_norm, fun = "MinProb", q = 0.01)
plot_imputation(data_norm, data_imp)
data_diff_manual <- test_diff(data_imp, type = "manual," test = c("t-
    SYID1_vs_WT1," "tSYID1_vs_YFP.Tb1","tSYID1_vs_LTI6B.Tb1","tSYID2_
    vs_WT2", "tSYID2_vs_YFP.Tb2","tSYID2_vs_LTI6B.Tb2"))
dep <- add_rejections(data_diff_manual, alpha = 0.05, lfc = log2(1.5))
plot_pca(dep, x = 1, y = 2, n = 500, point_size = 4)
ab<-get_results(dep)
write.csv(ab,"tSYID_BASL-BRXL2_MS6226-MS5931_PD/MQ results.csv")
```

CI is a metric designed to evaluate the enrichment reliability of protein candidates identified in proximity labeling experiments. It is defined as the sum of normalized peptide spectrum match (PSM) ratios comparing a test condition (tSYID-BASL/BRXL2) against two reference controls–wild type (WT) and YFP-TurboID. The formula is CI = (avePSM+1_tSYID-BASL/BRXL2/avePSM+1_WT) + (avePSM+1_tSYID-BASL/BRXL2/avePSM+1_YFP-TurboID)–where avePSM+1 represents the average PSM count plus one (to avoid division by zero). A higher CI indicates stronger and more confident enrichment relative to both control backgrounds.

Yeast Two-Hybrid Assays. The CDS of BASL, BRXL2, AGC1-9 were fused to the GAL4-activation domain or GAL4-binding domain and cloned into the pGBKT7 or pGADT7 vectors by LR reaction. These constructs were transformed into *Saccharomyces cerevisiae* strain Y187 and Y2HGold (Yeastmaker Yeast Transformation System 2, Clontech), and transformants were selected using colony PCR. Y187 and Y2HGold were mated in 4 mL 2× YPDA medium at 30 °C for 18 to 22 h. The resulting culture containing diploid yeasts was diluted and dropped on DDO medium (SD-Leu/-Trp) and QDO medium (SD-Leu/-Trp/-His/-Ade) and incubated at 30 °C for 3 d before photos were taken. Autoactivation assays have been performed for each bait and prey construct with corresponding empty vector to exclude potential false positives.

Split-YFP Assays for Protein-to-Protein Interaction In Planta. Split-YFP experiments involved transient protein expression in *N. benthamiana* leaves, which were infiltrated with *Agrobacterium* carrying the appropriate constructs, as described above. Leaves were collected for microscopic imaging 48 h after infiltration. Imaging was conducted using a Leica SP8 confocal microscope. YFP fluorescence was excited using a 514 nm Argon laser and detected with a custom 522 to 545 nm band-pass emission filter.

Plant Phenotyping and Quantification. For plant phenotyping, seeds of wild-type and mutant lines were sown on 1/2 MS agar plates with 0.7% agar. After stratification at 4 °C for 2 d, the plates were transferred vertically to a growth chamber set to a 16-h light/8-h dark cycle. For dark treatments, plates were covered with a layer of aluminum foil. Three days later, hypocotyl length, angle, and root length were measured using ImageJ (Fiji) software.

Confocal Imaging. Confocal images were captured using a Leica SP8 microscope of plant cells expressing fluorescence-tagged proteins. The images included the adaxial side of 3-d-old cotyledons, hypocotyls, and roots. Cell outlines were highlighted with propidiumiodide (PI) staining, diluted 1:100. The excitation wavelengths were set at 488 nm for GFP, 514 nm for mVenus, and 594 nm for PI. Corresponding emissions were collected at 510 to 523 nm for GFP, 522 to 545 nm for mVenus, and 620 to 640 nm for PI. Images were false-colored and adjusted for brightness and contrast using ImageJ (Fiji) software.

Statistics. All statistical analyses were conducted with GraphPad Prism 8 Software. Data are presented as means ± SEM, unless otherwise indicated. To compare two normally distributed groups, unpaired two-tailed *t* tests were used. For multiple comparisons between normally distributed groups, one-way ANOVA followed by Tukey's post hoc test was used. Statistical significance was set at $P < 0.05$. The number of biological replicates (n) and specific statistical tests used are detailed in the figure legends.

Data, Materials, and Software Availability. Relevant mass spectrometry (MS) proteomics data have been deposited to MassIVE (Identifier: MSV000097001; ftp://massive-ftp.ucsd.edu/v09/MSV000097001/) (27). The MS raw data associated with tSYID-BASL/BRXL2, YFP-TurboID, LTI6B-TurboID, and WT samples are listed in *SI Appendix*, Table S1. All other data are included in the manuscript and/or supporting information.

ACKNOWLEDGMENTS. We extend our gratitude to Dr. Xue Pan from the University of Toronto for sharing the pGWB501-based TurboID-mVenus Gateway Binary Vectors. We also thank Dr. Bryce Nickels at Rutgers, The State University of New Jersey, for allowing us the use of the ÄKTA Fast Protein Liquid Chromatography (FPLC) facility. Additionally, we acknowledge the Waksman Institute Shared Imaging Facility at Rutgers for access to the confocal microscopes. Mass spectrometry analyses were performed by the Biological Mass Spectrometry Facility at Robert Wood Johnson Medical School and Rutgers University and partly supported by S10 OD025140. This work was supported by grants from the NIH R35G131827 to J.D. and R35GM125003 to U.V.P. and the NSF 1952823 and 2049642 to J.D.

1. E. B. Abrash, D. C. Bergmann, Asymmetric cell divisions: A view from plant development. *Dev. Cell* **16**, 783–796 (2009).
2. X. Guo, J. Dong, Protein polarization: Spatiotemporal precisions in cell division and differentiation. *Curr. Opin. Plant Biol.* **68**, 102257 (2022).
3. M. T. Butler, J. B. Wallingford, Planar cell polarity in development and disease. *Nat. Rev. Mol. Cell Biol.* **18**, 375–388 (2017).
4. L. V. Goodrich, D. Strutt, Principles of planar polarity in animal development. *Development* **138**, 1877–1892 (2011).
5. R. Hale, D. Strutt, Conservation of planar polarity pathway function across the animal kingdom. *Annu. Rev. Genet.* **49**, 529–551 (2015).
6. M. Nakamura, C. S. Kiefer, M. Grebe, Planar polarity, tissue polarity and planar morphogenesis in plants. *Curr. Opin. Plant Biol.* **15**, 593–600 (2012).
7. E. Benková *et al.*, Local, efflux-dependent auxin gradients as a common module for plant organ formation. *Cell* **115**, 591–602 (2003).
8. Y. Boutté, Y. Ikeda, M. Grebe, Mechanisms of auxin-dependent cell and tissue polarity. *Curr. Opin. Plant Biol.* **10**, 616–623 (2007).
9. S. Yoshida *et al.*, A SOSEKI-based coordinate system interprets global polarity cues in *Arabidopsis*. *Nat. Plants* **5**, 160–166 (2019).
10. M. van Dop *et al.*, Dix domain polymerization drives assembly of plant cell polarity complexes. *Cell* **180**, 427–439.e412 (2020).
11. J. Dong, C. A. MacAlister, D. C. Bergmann, BASL controls asymmetric cell division in *Arabidopsis*. *Cell* **137**, 1320–1330 (2009).
12. P. Marhava *et al.*, A molecular rheostat adjusts auxin flux to promote root protophloem differentiation. *Nature* **558**, 297–300 (2018).
13. C. Mansfield *et al.*, Ectopic BASL reveals tissue cell polarity throughout leaf development in *Arabidopsis thaliana*. *Curr. Biol.* **28**, 2638–2646.e34 (2018).
14. J. A. Fozard *et al.*, Localization of stomatal lineage proteins reveals contrasting planar polarity patterns in *Arabidopsis* cotyledons. *Curr. Biol.* **32**, 4967–4974.e65 (2022).
15. M. Bringmann, D. C. Bergmann, Tissue-wide mechanical forces influence the polarity of stomatal stem cells in *Arabidopsis*. *Curr. Biol.* **27**, 877–883 (2017).
16. A. Mair, S. L. Xu, T. C. Branon, A. Y. Ting, D. C. Bergmann, Proximity labeling of protein complexes and cell-type-specific organellar proteomes in *Arabidopsis* enabled by TurboID. *Elife* **8**, e47864 (2019).
17. Y. Zhang *et al.*, TurboID-based proximity labeling reveals that UBR7 is a regulator of N NLR immune receptor-mediated immunity. *Nat. Commun.* **10**, 3252 (2019).
18. D. Arora *et al.*, Establishment of proximity-dependent biotinylation approaches in different plant model systems. *Plant Cell* **32**, 3388–3407 (2020).
19. T. C. Branon *et al.*, Efficient proximity labeling in living cells and organisms with TurboID. *Nat. Biotechnol.* **36**, 880–887 (2018).
20. K. F. Cho *et al.*, Split-TurboID enables contact-dependent proximity labeling in cells. *Proc. Natl. Acad. Sci. U.S.A.* **117**, 12143–12154 (2020).
21. E. S. Wallner *et al.*, Spatially resolved proteomics of the *Arabidopsis* stomatal lineage identifies polarity complexes for cell divisions and stomatal pores. *Dev. Cell* **59**, 1096–1109.e95 (2024).
22. Y. Zhang, P. Wang, W. Shao, J. K. Zhu, J. Dong, The BASL polarity protein controls a MAPK signaling feedback loop in asymmetric cell division. *Dev. Cell* **33**, 136–149 (2015).
23. A. Huang *et al.*, Proximity labeling proteomics reveals critical regulators for inner nuclear membrane protein degradation in plants. *Nat. Commun.* **11**, 3284 (2020).
24. Y. Zhang, D. C. Bergmann, J. Dong, Fine-scale dissection of the subdomains of polarity protein Basl in stomatal asymmetric cell division. *J. Exp. Bot.* **67**, 5093–5103 (2016), 10.1093/jxb/erw274.

25. K. F. Cho *et al.*, Proximity labeling in mammalian cells with TurboID and split-TurboID. *Nat. Protoc.* **15**, 3971–3999 (2020).
26. M. V. Thompson, S. M. Wolniak, A plasma membrane-anchored fluorescent protein fusion illuminates sieve element plasma membranes in *Arabidopsis* and tobacco. *Plant Physiol.* **146**, 1599–1610 (2008).
27. J. Dong *et al.*, Split-TurboID identifies new functions of basal cell polarity in *Arabidopsis*. MassIVE. ftp://massive-ftp.ucsd.edu/v09/MSV000097001/. Deposited 30 January 2025.
28. B. C. Orsburn, Proteome discoverer–a community enhanced data processing suite for protein informatics. *Proteomes* **9**, 15 (2021).
29. Z. A. Chen, L. Fischer, J. Cox, J. Rappsilber, Quantitative cross-linking/mass spectrometry using isotope-labeled cross-linkers and MaxQuant. *Mol. Cell Proteomics* **15**, 2769–2778 (2016).
30. X. Guo, C. H. Park, Z. Y. Wang, B. E. Nickels, J. Dong, A spatiotemporal molecular switch governs plant asymmetric cell division. *Nat. Plants* **7**, 667–680 (2021).
31. X. Guo, X. Ding, J. Dong, Dichotomy of the BSL phosphatase signaling spatially regulates MAPK components in stomatal fate determination. *Nat. Commun.* **13**, 2438 (2022).
32. B. C. Willige *et al.*, D6PK AGCVIII kinases are required for auxin transport and phototropic hypocotyl bending in *Arabidopsis*. *Plant Cell* **25**, 1674–1688 (2013).
33. I. C. Barbosa, M. Zourelidou, B. C. Willige, B. Weller, C. Schwechheimer, D6 PROTEIN KINASE activates auxin transport-dependent growth and PIN-FORMED phosphorylation at the plasma membrane. *Dev. Cell* **29**, 674–685 (2014).
34. O. Hazelwood, M. A. Ashraf, Opposing polarity domains provide direction and play a role in cell division in plant growth. *Dev. Cell* **59**, 1091–1093 (2024).
35. M. H. Rowe, J. Dong, A. K. Weimer, D. C. Bergmann, A plant-specific polarity module establishes cell fate asymmetry in the *Arabidopsis* stomatal lineage. bioRxiv [Preprint] (2019). https://doi.org/10.1101/614636 (Accessed 19 April 2019).
36. A. Gadeyne *et al.*, The TPLATE adaptor complex drives clathrin-mediated endocytosis in plants. *Cell* **156**, 691–704 (2014).
37. E. J. Drdová *et al.*, The exocyst complex contributes to PIN auxin efflux carrier recycling and polar auxin transport in *Arabidopsis*. *Plant J.* **73**, 709–719 (2013).
38. M. Fendrych *et al.*, The *Arabidopsis* exocyst complex is involved in cytokinesis and cell plate maturation. *Plant Cell* **22**, 3053–3065 (2010).
39. T. Kinoshita *et al.*, *phot1* and *phot2* mediate blue light regulation of stomatal opening. *Nature* **414**, 656–660 (2001).
40. J. M. Christie, Phototropin blue-light receptors. *Annu. Rev. Plant Biol.* **58**, 21–45 (2007).
41. P. Gouguet *et al.*, Connecting the dots: From nanodomains to physiological functions of REMORINs. *Plant Physiol.* **185**, 632–649 (2020).
42. J. Hornbergs *et al.*, SEC14-GOLD protein PATELLIN2 binds IRON-REGULATED TRANSPORTER1 linking root iron uptake to vitamin E. *Plant Physiol.* **192**, 504–526 (2022).
43. H. Zhou *et al.*, Patellin1 negatively modulates salt tolerance by regulating PM Na+/H+ antiport activity and cellular redox homeostasis in *Arabidopsis*. *Plant Cell Physiol.* **59**, 1630–1642 (2018).
44. W. Bae *et al.*, AKR2A-mediated import of chloroplast outer membrane proteins is essential for chloroplast biogenesis. *Nat. Cell Biol.* **10**, 220–227 (2008).
45. D. H. Kim *et al.*, Cytosolic targeting factor AKR2A captures chloroplast outer membrane-localized client proteins at the ribosome during translation. *Nat. Commun.* **6**, 6843 (2015).
46. T. V. Humphrey *et al.*, PERK–KIPK–KCBP signalling negatively regulates root growth in *Arabidopsis thaliana*. *J. Exp. Bot.* **66**, 71–83 (2014).
47. J. K. Polko *et al.*, SHOU4 proteins regulate trafficking of cellulose synthase complexes to the plasma membrane. *Curr. Biol.* **28**, 3174–3182.e76 (2018).
48. A. Houbaert *et al.*, POLAR-guided signalling complex assembly and localization drive asymmetric cell division. *Nature* **563**, 574–578 (2018).
49. L. Wang *et al.*, Connected function of PRAF/RLD and GNOM in membrane trafficking controls intrinsic cell polarity in plants. *Nat. Commun.* **13**, 7 (2022).
50. G. Shen *et al.*, ANKYRIN REPEAT-CONTAINING PROTEIN 2A Is an essential molecular chaperone for peroxisomal membrane-bound ASCORBATE PEROXIDASE3 in *Arabidopsis*. *Plant Cell* **22**, 811–831 (2010).
51. Y. Zhang, S. McCormick, AGCVIII kinases: At the crossroads of cellular signaling. *Trends Plant Sci.* **14**, 689–695 (2009).
52. I. S. Day, C. Miller, M. Golovkin, A. S. N. Reddy, Interaction of a kinesin-like calmodulin-binding protein with a protein kinase. *J. Biol. Chem.* **275**, 13737–13745 (2000).
53. Y. Xiao *et al.*, KIPK and KIPK-LIKE1 suppress overbending during negative hypocotyl gravitropic growth. bioRxiv [Preprint] (2024). https://doi.org/10.1101/2024.05.24.595653 (Accessed 28 May 2024).
54. Y. Mao *et al.*, Application of the CRISPR–Cas system for efficient genome engineering in plants. *Mol. Plant* **6**, 2008–2011 (2013).
55. L. J. Pillitteri, K. M. Peterson, R. J. Horst, K. U. Torii, Molecular profiling of stomatal meristemoids reveals new component of asymmetric cell division and commonalities among stem cell populations in *Arabidopsis*. *Plant Cell* **23**, 3260–3275 (2011).
56. Y. Gong *et al.*, Quantitative and dynamic cell polarity tracking in plant cells. *New Phytol.* **230**, 867–877 (2021).
57. E.-J. Kim *et al.*, Cell type–specific attenuation of brassinosteroid signaling precedes stomatal asymmetric cell division. *Proc. Natl. Acad. Sci. U.S.A.* **120**, e2303758120 (2023).
58. E.-S. Wallner *et al.*, Spatially resolved proteomics of the *Arabidopsis* stomatal lineage identifies polarity complexes for cell divisions and stomatal pores. *Dev. Cell* **59**, 1096–1109.e95 (2024).
59. E. S. Wallner, L. Dolan, D. C. Bergmann, *Arabidopsis* stomatal lineage cells establish bipolarity and segregate differential signaling capacity to regulate stem cell potential. *Dev. Cell* **58**, 1643–1656. e45 (2023).
60. K. Haga, L. Frank, T. Kimura, C. Schwechheimer, T. Sakai, Roles of AGCVIII Kinases in the hypocotyl phototropism of *Arabidopsis* seedlings. *Plant Cell Physiol.* **59**, 1060–1071 (2018).
61. A. Muroyama, D. Bergmann, Plant cell polarity: Creating diversity from inside the box. *Annu. Rev. Cell Dev. Biol.* **35**, 309–336 (2019).
62. J. J. Ramalho, V. A. S. Jones, S. Mutte, D. Weijers, Pole position: How plant cells polarize along the axes. *Plant Cell* **34**, 174–192 (2021).
63. U. Tepass, The apical polarity protein network in *Drosophila* epithelial cells: Regulation of polarity, junctions, morphogenesis, cell growth, and survival. *Annu. Rev. Cell Dev. Biol.* **28**, 655–685 (2012).
64. A. Riga, V. G. Castiglioni, M. Boxem, New insights into apical–basal polarization in epithelia. *Curr. Opin. Cell Biol.* **62**, 1–8 (2020).
65. A. Carmena, The case of the scribble polarity module in asymmetric neuroblast division in development and tumorigenesis. *Int. J. Mol. Sci.* **21**, 2865 (2020).
66. A. Suzuki, S. Ohno, The PAR-aPKC system: Lessons in polarity. *J. Cell Sci.* **119**, 979–987 (2006).
67. A. Wodarz, I. Näthke, Cell polarity in development and cancer. *Nat. Cell Biol.* **9**, 1016–1024 (2007).
68. D. Zhang *et al.*, Opposite polarity programs regulate asymmetric subsidiary cell divisions in grasses. *Elife* **11**, e79913 (2022).
69. M. R. Facette, L. G. Smith, Division polarity in developing stomata. *Curr. Opin. Plant Biol.* **15**, 585–592 (2012).
70. A. Muroyama, Y. Gong, K. S. Hartman, D. C. Bergmann, Cortical polarity ensures its own asymmetric inheritance in the stomatal lineage to pattern the leaf surface. *Science* **381**, 54–59 (2023).
71. A. Muroyama, Y. Gong, D. C. Bergmann, Opposing, polarity-driven nuclear migrations underpin asymmetric divisions to pattern *Arabidopsis* stomata. *Curr. Biol.* **30**, 4549–4552 (2020).
72. E. Truernit, H. Bauby, K. Belcram, J. Barthélémy, J. C. Palauqui, OCTOPUS, a polarly localised membrane-associated protein, regulates phloem differentiation entry in *Arabidopsis thaliana*. *Development* **139**, 1306–1315 (2012).
73. X. Zhang *et al.*, OCTOPUS regulates BIN2 to control leaf curvature in Chinese cabbage. *Proc. Natl. Acad. Sci. U.S.A.* **119**, e2208978119 (2022).
74. J. X. He, J. M. Gendron, Y. Yang, J. Li, Z. Y. Wang, The GSK3-like kinase BIN2 phosphorylates and destabilizes BZR1, a positive regulator of the brassinosteroid signaling pathway in *Arabidopsis*. *Proc. Natl. Acad. Sci. U.S.A.* **99**, 10185–10190 (2002).
75. J. Li *et al.*, Modulation of BIN2 kinase activity by HY5 controls hypocotyl elongation in the light. *Nat. Commun.* **11**, 1592 (2020).
76. S. Bernardo-García *et al.*, BR-dependent phosphorylation modulates PIF4 transcriptional activity and shapes diurnal hypocotyl growth. *Genes Dev.* **28**, 1681–1694 (2014).
77. G. Vert, C. L. Walcher, J. Chory, J. L. Nemhauser, Integration of auxin and brassinosteroid pathways by Auxin Response Factor 2. *Proc. Natl. Acad. Sci. U.S.A.* **105**, 9829–9834 (2008).
78. T.-W. Kim *et al.*, Mapping the signaling network of BIN2 kinase using TurboID-mediated biotin labeling and phosphoproteomics. *Plant Cell* **35**, 975–993 (2023).
79. T. Stanislas *et al.*, *Arabidopsis* D6PK is a lipid domain-dependent mediator of root epidermal planar polarity. *Nat. Plants* **1**, 15162 (2015).
80. S. Tan *et al.*, The lipid code-dependent phosphoswitch PDK1-D6PK activates PIN-mediated auxin efflux in *Arabidopsis*. *Nat. Plants* **6**, 556–569 (2020).
81. K. X. Zhang, H. H. Xu, T. T. Yuan, L. Zhang, Y. T. Lu, Blue-light-induced PIN3 polarization for root negative phototropic response in *Arabidopsis*. *Plant J.* **76**, 308–321 (2013).
82. Z. Zhang *et al.*, KETCH1 imports HYL1 to nucleus for miRNA biogenesis in *Arabidopsis*. *Proc. Natl. Acad. Sci. U.S.A.* **114**, 4011–4016 (2017).
83. L. Xia, M. Mar Marques-Bueno, R. Karnik, Trafficking SNARE SYP132 partakes in auxin-associated root growth. *Plant Physiol.* **182**, 1836–1840 (2020).
84. L. Synek *et al.*, Plasma membrane phospholipid signature recruits the plant exocyst complex via the EXO70A1 subunit. *Proc. Natl. Acad. Sci. U.S.A.* **118**, e2105287118 (2021).
85. S. D'Alessandro *et al.*, Phosphorylation of p23–1 cochaperone by protein kinase CK2 affects root development in *Arabidopsis*. *Sci. Rep.* **9**, 9846 (2019).
86. M. Adamowski *et al.*, A functional ftudy of AUXILIN-LIKE1 and 2, two putative clathrin uncoating factors in *Arabidopsis*. *Plant Cell* **30**, 700–716 (2018).
87. J. Deng, X. Wang, Z. Liu, T. Mao, The microtubule-associated protein WDL4 modulates auxin distribution to promote apical hook opening in *Arabidopsis*. *Plant Cell* **33**, 1927–1944 (2021).
88. K. Schaefer *et al.*, WAVE-DAMPENED2-LIKE4 modulates the hyper-elongation of light-grown hypocotyl cells. *Plant Physiol.* **192**, 2687–2702 (2023).
89. W. M. Leu, X. L. Cao, T. J. Wilson, D. P. Snustad, N. H. Chua, Phytochrome A and phytochrome B mediate the hypocotyl-specific downregulation of TUB1 by light in *arabidopsis*. *Plant Cell* **7**, 2187–2196 (1995).
90. B. Favery *et al.*, *Arabidopsis* formin AtFH6 is a plasma membrane-associated protein upregulated in giant cells induced by parasitic nematodes. *Plant Cell* **16**, 2529–2540 (2004).
91. H. Zhou *et al.*, Patellin protein family functions in plant development and stress response. *J. Plant Physiol.* **234–235**, 94–97 (2019).
92. M. H. Le, Y. Cao, X. C. Zhang, G. Stacey, LIK1, a CERK1–interacting kinase, regulates plant immune responses in *Arabidopsis*. *PLoS One* **9**, e102245 (2014).
93. M. Ke *et al.*, Salicylic acid regulates PIN2 auxin transporter hyperclustering and root gravitropic growth via Remorin-dependent lipid nanodomain organisation in *Arabidopsis thaliana*. *New Phytol.* **229**, 963–978 (2021).
94. A. Perraki *et al.*, REM1.3's phospho-status defines its plasma membrane nanodomain organization and activity in restricting PVX cell-to-cell movement. *PLoS Pathog.* **14**, e1007378 (2018).
95. T. V. Humphrey *et al.*, PERK-KIPK-KCBP signalling negatively regulates root growth in *Arabidopsis thaliana*. *J. Exp. Bot.* **66**, 71–83 (2015).
96. N. F. Silva, D. R. Goring, The proline-rich, extensin-like receptor kinase-1 (PERK1) gene is rapidly induced by wounding. *Plant Mol. Biol.* **50**, 667–685 (2002).
97. S. Krishnakumar, D. G. Oppenheimer, Extragenic suppressors of the *Arabidopsis* zwi-3 mutation identify new genes that function in trichome branch formation and pollen tube growth. *Development* **126**, 3079–3088 (1999).
98. D. G. Oppenheimer *et al.*, Essential role of a kinesin-like protein in *Arabidopsis* trichome morphogenesis. *Proc. Natl. Acad. Sci. U.S.A.* **94**, 6261–6266 (1997).
99. Y. Xiao *et al.*, The protein kinases KIPK and KIPK-LIKE1 suppress overbending during negative hypocotyl gravitropic growth in *Arabidopsis*. *Plant Cell* **37**, koaf056 (2025).
100. K. Kim *et al.*, Phytochromes inhibit hypocotyl negative gravitropism by regulating the development of endodermal amyloplasts through phytochrome-interacting factors. *Proc. Natl. Acad. Sci. U.S.A.* **108**, 1729–1734 (2011).
101. M. Nakamura, T. Nishimura, M. T. Morita, Bridging the gap between amyloplasts and directional auxin transport in plant gravitropism. *Curr. Opin. Plant Biol.* **52**, 54–60 (2019).
102. P. Li *et al.*, LAZY1 controls rice shoot gravitropism through regulating polar auxin transport. *Cell Res.* **17**, 402–410 (2007).
103. J. Chen *et al.*, Amyloplast sedimentation repolarizes LAZYs to achieve gravity sensing in plants. *Cell* **186**, 4788–4802.e15 (2023).
104. P. Marhava *et al.*, Plasma membrane domain patterning and self-reinforcing polarity in *Arabidopsis*. *Dev. Cell* **52**, 223–235.e225 (2020).
105. A. Gupta, M. Singh, A. M. Jones, A. Laxmi, Hypocotyl directional growth in *Arabidopsis*: A complex trait. *Plant Physiol.* **159**, 1463–1476 (2012).
106. Z.-P. Wang *et al.*, Egg cell-specific promoter-controlled CRISPR/Cas9 efficiently generates homozygous mutants for multiple target genes in *Arabidopsis* in a single generation. *Genome Biol.* **16**, 144 (2015).